Rare Met. (2023) 42(10):3326–3336
https://doi.org/10.1007/s12598-023-02415-9

RARE METALS

LETTER

MOF-derived nitrogen-doped iron–nickel oxide carbon nanotubes as efficient oxygen electrocatalyst for long-life rechargeable zinc–air batteries

Tao Zhao, Yu-Hang Wu, Zhi-Rong Song, Xue Wang, Rui-Lian Yin, Hui Xu*, Hui Cui, Xie-Hong Cao*, Jun-Kuo Gao*

Received: 6 February 2023 / Revised: 2 March 2023 / Accepted: 14 March 2023 / Published online: 4 September 2023

Electrocatalysts with high activities are crucial for high-energy-density Zn-air batteries. However, the sluggish kinetics of oxygen evolution reaction (OER) and oxygen reduction reaction (ORR) on the electrocatalysts hindered the development of Zn-air batteries. Herein, a new class of MOF-derived nitrogen-doped carbon nanotubes encapsulated with bimetallic oxide (FeNiO@NCNT) through facile pyrolysis strategy is reported. The FeNiO@NCNT exhibits high catalytic activities for both OER and ORR. In particular, lattice oxygen and OH^- in FeNiO@NCNT provide more active sites (except metal active sites) for OER, making FeNiO@NCNT has more excellent OER performance than other catalysts ($E_{j=10}$ = 205 mV). As an OER and ORR bifunctional catalyst, the rechargeable Zn-air batteries based on FeNiO@NCNT exhibit a higher discharge power density of 124.29 $mW{\cdot}cm^{-2}$, along with low charge–discharge polarization and superior cycling stability of 440 h at 20 $mA{\cdot}cm^{-2}$ with no expand in polarization. This work demonstrates FeNiO@NCNT as promising potential catalyst for the practical application in various integrated energy systems.

The development of efficient energy conversion and storage technologies is one of the key steps to solve energy shortages and improve human life style [1–6]. Given the high theoretical energy density, high power, high safety and low cost, metal–air batteries (such as Zn-air batteries) have been considered as promising renewable and sustainable energy sources [7–11]. The energy store devices generate electrical energy through the oxygen reversible reaction, reacting at metal part (anode) and air-breathing cathode [12–18]. However, the sluggish kinetics of OER and ORR lead to low-power density and poor stability of these devices, which limits their large-scale practical applications [19–23]. To date, the noble metal-based catalysts (such as Pt/C, IrO_x and RuO_x) used in the cathodes of metal–air batteries are not only rare and precious, but their catalytic bifunctionality and stability are also in insufficient [24–27]. Thus, the key requirement for successful implementation of metal-air batteries is to develop the bifunctional electrocatalysts with low cost, efficient catalytic activity and stability to boost the kinetics for both OER and ORR [28–30].

Recently, nonprecious metal-based materials have become potential candidates to replace noble metal-

Supplementary Information The online version contains supplementary material available at https://doi.org/10.1007/s12598-023-02415-9.

T. Zhao, Y.-H. Wu, Z.-R. Song, X. Wang, J.-K. Gao*
School of Materials Science and Engineering, Institute of Functional Porous Materials, Zhejiang Sci-Tech University, Hangzhou 310018, China
e-mail: jkgao@zstu.edu.cn

R.-L. Yin, X.-H. Cao*
College of Materials Science and Engineering, Pinghu Institute of Advanced Materials, Zhejiang University of Technology, Hangzhou 310014, China
e-mail: gcscaoxh@zjut.edu.cn

H. Xu*
Institute of Optoelectronic Materials and Devices, China Jiliang University, Hangzhou 310018, China
e-mail: huixu@cjlu.edu.cn

H. Cui
Physics Division, Argonne National Laboratory, Lemont, IL 60439, USA

H. Cui
Department of Chemistry and International Institute for Nanotechnology (IIN), Northwestern University, Evanston, IL 60208, USA

supported catalysts [31–33]. The transition metal (such as Co, Fe and Ni)-based materials with low cost, abundant reserves and fast kinetics have been attracted widespread attention as promising electrocatalysts [34–38]. Especially, bimetal-based electrocatalysts exhibit superior electrocatalytic activities for oxygen catalysis have been widely reported [39–42]. In recent years, metal–organic frameworks (MOFs), which assembled by metal moieties and organic ligands, are potential precursors to develop carbon-based electrocatalysts with bimetallic active sites [43–46]. The two metal units can not only synergistic to optimize the electronic structure, but also increase the charge carrier density of the catalyst [47, 48]. In addition, to improve the conductivity of the material, lots of efforts have been contributed to explore the MOF-based carbon materials (e.g., nanoparticles, nanosheets and nanotubes) with large specific surface area and intrinsic high conductivity [49–54]. However, the weak catalytic performances of pure carbon materials greatly reduce the utilization efficiency of the catalysts. Thus, the modification can be added such as heteroatom functionalization and defect engineering based on superior modifiability of MOF precursors [55–57]. Although great progress has been made in MOF-derived bimetallic electrocatalysts, it is essential for high-output air batteries to synergistically optimize the relationship between the active catalytic sites and the conductivity of the electrocatalysts [58–61].

Herein, we present a scalable synthesis strategy based on pyrolytic oxidation strategy to fabricate a new class of nitrogen-doped carbon nanotubes encapsulated with bimetallic oxide derived from metal–organic frameworks as a bifunctional electrocatalytic catalyst for rechargeable Zn–air batteries. In view of the synergistic effect through the nanotube structure and bimetallic oxide doping effects, the obtained electrocatalyst shows outstanding OER activities with a large mass activity of 734.7 $A \cdot g^{-1}$ at an overpotential of 300 mV. The FeNiO@NCNT-based Zn–air battery presents impressive performance including the high-power density of 129.24 $mW \cdot cm^{-1}$ and excellent stability (maintain over 440 h without obvious capacity degradation), suggesting its application potential in energy conversion devices. Therefore, this work provides an advanced oxygen catalyst and a new direction for the reasonable exploration of cathode catalysts for zinc–air batteries.

As illustrated in Scheme 1, the general strategy is used for the fabrication of bifunctional FeNiO@NCNT catalyst, which is based on a facile two-step pyrolysis process. The precursors were synthesized through self-assembly of metal ions and sodium dicyanamide with addition of urotropine. The obtained rod-shaped single-metal and bimetallic precursors were named Fe-MOF-1, Ni-MOF-1 and FeNi-MOF-1, respectively. SEM images and XRD patterns of precursors both showed the similar results with previously reported (Figs. S1, S2) [62, 63]. XRD results show that FeNi-MOF-1 is a composite of Fe-MOF-1 and Ni-MOF-1, which proves that the bimetallic FeNi-coordinated MOF was successfully synthesized. Subsequently, the M@NCNT (M = Fe, Ni or FeNi) was obtained through pyrolysis at 800 °C under N_2 atmosphere. Remarkable, the FeNi alloy NPs that served as catalytic sites grew in NCNT during the pyrolysis, since the undesired metal particles were removed by acid leaching. To further enhance the performance of electrocatalysis, the M@NCNT following treated in air at 350 °C to oxidize some of alloy metals. As a result, the MO@NCNT was successfully synthesized.

SEM and TEM images demonstrate a nanotube structure of M@NCNT, which is formed during the pyrolysis with the metal nanoparticles encapsulated in the carbon layer as shown in Fig. S3. With increase in pyrolysis temperature, dicyandiamide decomposed and converted to graphitic carbon nitride, which is similar to the conversion of melamine to C_3N_4 [64]. Subsequently, the N-doped nanotubes were formed by circulating of NH_3 decomposed from C_3N_4 in carbon. As shown in Fig. 1a–c, the nanotube structures of MO@NCNT maintain pristine structures without collapse after oxidation. Remarkably, the nanotube wall of MO@NCNT was thickened significantly, as shown in TEM images (Fig. 1d–f), which not only provided large contact interface to improve the conductivity and increase electron transfer rates, but also protected metal active centers to enhance the catalytic efficiency. Meanwhile, FeNiO@NCNT exhibited more densely and wrapped carbon nanotubes with metal nanoparticles (around 100 nm) compared to FeO@NCNT and NiO@NCNT, which were favorable for transferring of electrolyte and gas diffusion.

The lattice spacing of 0.207 nm is detected for the selected area in high-resolution transmission electron microscopy (HRTEM) image (inset in Fig. 1f), which is consistent with the (111) crystal plane of FeNi alloy [65, 66]. However, TEM elemental mapping shows that O signal is uniformly distributed within nanoparticles apart from Fe and Ni signals (Fig. 1g–j). The result suggests that the metal nanoparticles in FeNiO@NCNT composed of FeNi alloy and corresponding partial oxides. Some O signals are displayed on the carbon nanotubes, which is attributed to the partial oxidation of the nanotubes. In addition, uniform C and N signals were detected in the carbon nanotubes in Fig. S4, indicating that the N element was indeed doped into the carbon nanotubes. XRD patterns of MO@NCNT were used to confirm the catalytic sites embedded in nanotubes. As shown in Fig. S5, the diffraction peak at about 26° assigned to the (002) plane of graphitic carbon (PDF No. 75-1621). However, the MO@NCNT only shows the diffraction peak of iron–nickel alloy or metal element (about 43° and 52°

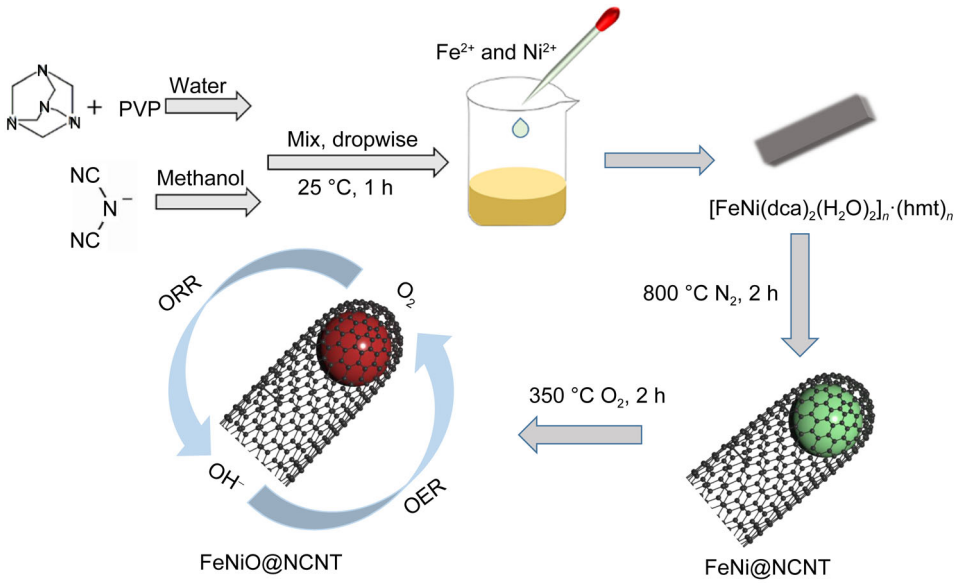

Scheme 1 Synthetic process of FeNiO@NCNT

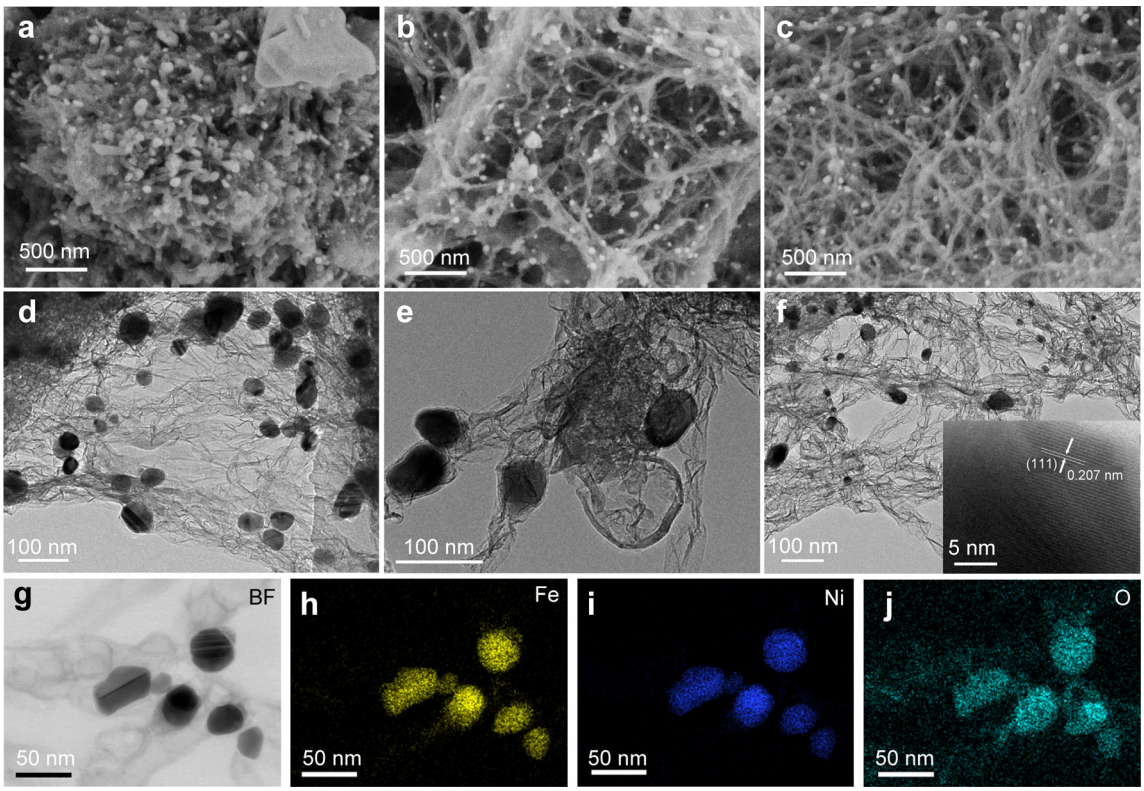

Fig. 1 a–c SEM images of FeO@NCNT, NiO@NCNT and FeNiO@NCNT, respectively; **d–f** TEM images of FeO@NCNT, NiO@NCNT and FeNiO@NCNT, respectively (high-resolution TEM image of FeNiO@NCNT); **g–j** elemental mappings of FeNiO@NCNT

corresponding to the plane of (111) and (200), respectively (PDF No. 47-1405)). Thus, metallic catalytic sites are oxidized partially, which may be more favorable for oxygen catalysis.

XPS was further conducted to investigate the elemental compositions and chemical states of MO@NCNT. Figure 2 shows the high-resolution Fe 2p and Ni 2p spectra of FeNiO@NCNT, respectively, indicating the presence of

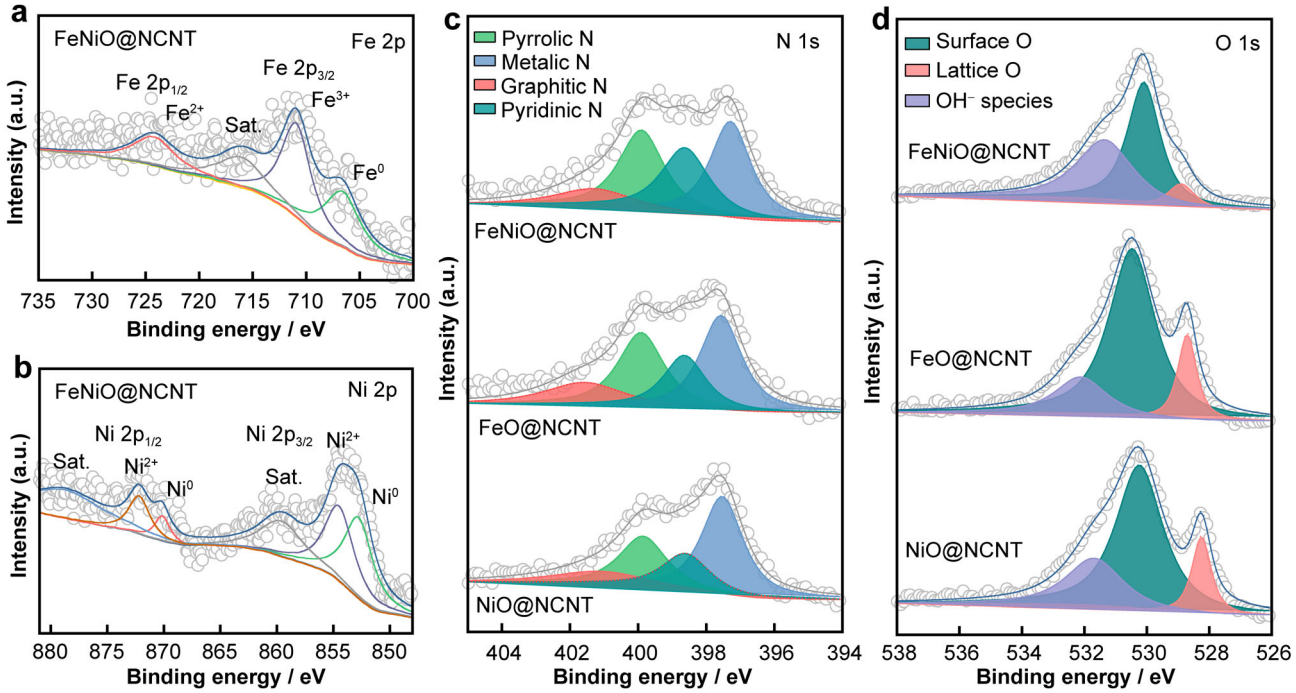

Fig. 2 XPS spectra of MO@NCNT: **a** Fe 2p and **b** Ni 2p spectra of FeNiO@NCNT, **c** N 1s and **d** O 1s spectra of MO@NCNT

the metals in oxidized state on the surface of FeNiO@NCNT. The typical characteristic peaks at about 706 and 852.7 eV in Fe $2p_{3/2}$ and Ni $2p_{3/2}$, respectively, can be assigned to metallic alloy [67, 68]. The peaks of Fe^{2+} and Fe^{3+} (about 710.9 and 724.8 eV) could be fitted, indicating the partly oxidized surface of metallic Fe (Fig. 2a) [69, 70]; meanwhile, the peaks of Ni^{2+} also can be detected at about 853.7 and 872 eV at Ni^{2+} $2p_{3/2}$ and Ni^{2+} $2p_{1/2}$ (Fig. 2b) [71, 72], respectively, which is attributed to the partial oxidation of metallic Ni. The presence of partially oxidized metal particles may provide more active sites, which have a significant effect on the activity of the catalyst. As shown in Fig. 2c, the high-resolution N 1s spectra disclose four N species, including M–N (~ 397.4 eV), pyridinic-N (~ 398.4 eV), pyrrolic-N (~ 399.7 eV) and graphitic-N (~ 401.2 eV), respectively [73, 74]. Remarkable, FeNiO@NCNT exhibits the highest content of pyridinic-N, which plays an important role for OER and ORR [75, 76]. Furthermore, the O 1s spectrum presents three types O peaks at around 528.5, 530.5 and 531.5 eV, which correspond to lattice oxygen, surface oxygen and OH^- species, respectively (Fig. 2d) [77]. Compared to FeO@NCNT and NiO@NCNT, the higher concentration of OH^- species in FeNiO@NCNT demonstrates that bimetallic ions are favorable to the generation of high-density extra oxygen vacancies, which may lead to the faster reaction rate of FeNiO@NCNT in the oxygen electrode reactions [78].

Raman spectroscopy was applied to study structural defects and graphitization levels of the prepared catalysts based on the intensity ratio I_G/I_D of defect (D-band) and graphitic (G-band) carbon around 1350 and 1590 cm^{-1} [79]. As shown in Fig. S6, bimetallic NCNT showed higher I_G/I_D for both M@NCNT and MO@NCNT compared to single-metal NCNT, suggesting higher degree of graphitization for bimetallic NCNT. Remarkably, the value of I_G/I_D for FeNiO@NCNT is 2.78, which is the highest among all samples, demonstrated that the superior conductivity for FeNiO@NCNT is due to its highly graphitized carbon nanotubes with less defects. This result is consistent with the observations in SEM and TEM images, in which the nanotubes of FeNiO@NCNT are tidier, while the nanotubes in FeO@NCNT and NiO@NCNT have many particles coexisting. Furthermore, FeNiO@NCNT has lower I_G/I_D values than most carbon materials, indicating that a large number of defects in the catalyst were formed due to nitrogen doping. These defect centers provide active sites for the OER and ORR process to ensure better electrocatalytic performance.

The catalyst-specific surface area is critical to the catalytic activity, for which all samples were Brunauer–Emmett–Teller (BET) explored. The specific surface area and porosity of M@NCNT and MO@NCNT were explored by N_2 adsorption–desorption isotherm shown in Figs. S7 and S8. BET results of FeNiO@NCNT are shown in Fig. 3a. All samples showed a type-IV isotherm with obvious hysteresis. In particular, the bimetallic FeNi-

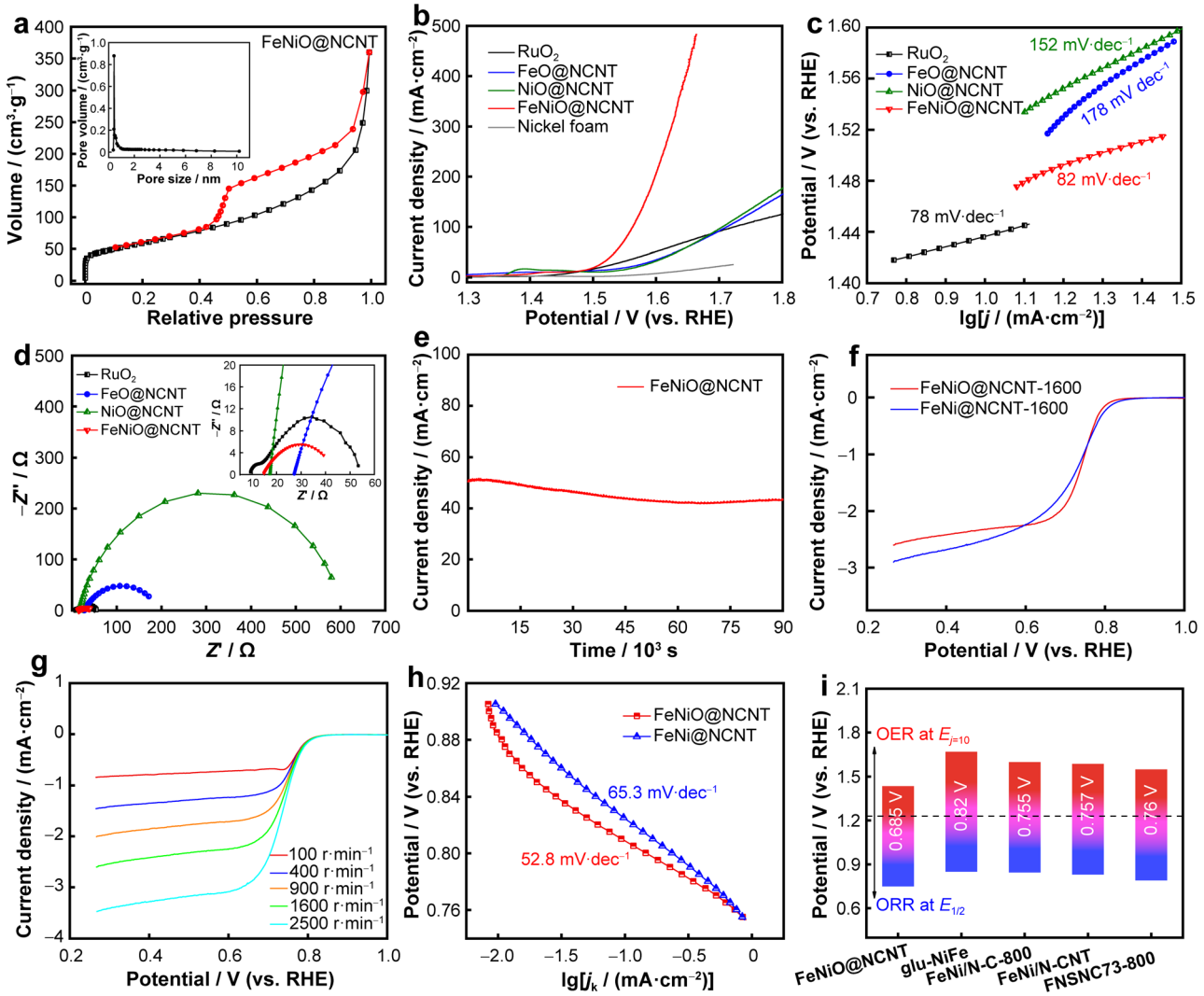

Fig. 3 **a** Nitrogen sorption isotherm of FeNiO@NCNT, **b** LSV polarization curves on NF, **c** corresponding Tafel plots of MO@NCNT samples and RuO_2 in 1.0 mol·L^{-1} KOH solution, **d** *iR* compensation of MO@NCNT, **e** chronoamperometric response of FeNiO@NCNT, **f** LSV curves of FeNi@NCNT and FeNiO@NCNT in O_2-saturated 0.1 mol·L^{-1} KOH solution at 1600 r·min^{-1}, **g** LSV curves of FeNiO@NCNT in O_2-saturated 0.1 mol·L^{-1} KOH solution at various rotation rates, **h** Tafel slopes from LSV curves at 1600 r·min^{-1} and **i** values of ΔE ($\Delta E = E_{j=10} - E_{1/2}$) of FeNiO@NCNT and other control samples

coordinated catalyst shows an excellent specific surface area, which also proves its better performance than other samples. Among them, the specific surface areas of FeNi and FeNiO are 218.9 and 212.6 m^2·g^{-1}, respectively. The slight reduction of the specific surface area of FeNi in the process of oxidation to FeNiO is attributed to the intervention of O to occupy a certain coordination. The thickening of carbon nanotubes during the oxidation process is also directly related to the reduction of specific surface area, which is consistent with the results of SEM and TEM. The BET results for all catalysts are listed in Table S1. After oxidation, the specific surface area of FeNiO@NCNT without any changed while that of FeO@NCNT and NiO@NCNT decreased. Such rich porous structures enable the diffusion of ions in electrolyte and efficient transport of reaction species to enhance electrocatalysis.

The oxygen catalytic activity of M@NCNT and MO@NCNT was analyzed by OER and ORR tests. In OER region, the electrocatalytic performance was evaluated in conventional three-electrode system in 1 mol·L^{-1} KOH solution. M@NCNT and MO@NCNT were deposited onto Ni foam (NF) electrode. The linear sweep voltammetry (LSV) polarization curves of MO@NCNT on NF are shown in Fig. 3b, where FeNiO@NCNT exhibits outstanding performance. FeNiO@NCNT only needs overpotential of 205 mV to achieve current densities of 10 mA·cm^{-2} (Fig. S9). Its OER activity is significantly higher than RuO_2 (240 mV at 10 mA·cm^{-2}). At high

current densities, the OER activity of FeNiO@NCNT (305 mV at 50 mA·cm^{-2} and 332 mV at 100 mA·cm^{-2}) is not only higher than that of RuO_2 (368 mV at 50 mA·cm^{-2} and 494 mV at 100 mA·cm^{-2}), but also higher than that of FeNi@NCNT (337 mV at 50 mA·cm^{-2} and 406 mV at 100 mA·cm^{-2}) (Fig. S10a). OER performance of all catalysts is shown in Table S2. In particular, the current density of FeNiO@NCNT can reach 500 mA·cm^{-2}, which is much higher than other catalysts, including RuO_2 and FeNi@NCNT. The loading of all catalysts on NF was 0.03 mg·cm^{-2}. When the overpotential is 300 mV, FeNiO@NCNT shows great potential to achieve a high-quality current ratio of 734.7 A·g^{-1}.

Metal centers are traditionally considered to be the main active sites of metal oxides. However, the contribution of lattice oxygen and OH^- to OER is neglected. In fact, lattice oxygen and OH^- also participate in the catalytic reaction and can significantly reduce the overpotential of OER [80]. In an alkaline environment, lattice oxygen and OH^- on the surface of the catalyst can directly participate in OER and react with hydroxide ions adsorbed on the metal center to form H_2O_2 [81]. Owing to the participation of lattice hydroxide species, high surface OH^- coverage is not required to achieve low OER overpotential. Moreover, during the oxygen release process, the formed oxygen vacancies can be replenished by another OH^- produced by the decomposition of H_2O_2. The excellent OER performance of FeNiO@NCNT is partly attributed to the synergistic catalysis of the bimetallic FeNi alloy. The other part is attributed to the large amount of lattice oxygen and OH^- in the oxides participating in the catalytic reaction.

The Tafer slope is shown in Figs. 3c, S10b. It can be clearly seen that FeNiO@NCNT (82 mV·dec^{-1}) is only worse than RuO_2 (78 mV·dec^{-1}), which is significantly better than other catalysts. The electrochemical impedance spectroscopy (EIS) in Fig. 3d shows that FeNiO@NCNT (26.5 Ω) and RuO_2 (54 Ω) provide lower charge transfer resistance (R_{ct}) than other samples. The reaction resistance of FeNiO@NCNT (26.5 Ω) is smaller than FeNi@NCNT (30 Ω) (Fig. S10c). It fully demonstrates that the synergistic effect of the bimetallic-doped oxides, while the participation of oxygen further optimizes the electronic structure, promotes the transfer of electrons and improves the electrochemical activity. In order to investigate the stability of the catalyst FeNiO@NCNT, it was measured using a chronoamperometry method. As shown in Fig. 3e, the catalyst remained stable (85%) after 90,000 s of continuous operation. After a long period of work, the FeNiO@NCNT has not been decomposed, and its shape remains intact (Fig. S11). It is shown that the metal oxide can maintain high-efficiency activity for a long time in an alkaline solution (1 mol·L^{-1} KOH). The protection of the carbon layer is an important reason for the stability of the metal oxide. It shows that while maintaining high activity of oxide, it overcomes the disadvantage of poor stability. The electrochemically active surface area (ECSA) and double layer capacitor capacitance C_{dl} calculation results of MO@NCNT are shown in Figs. S12–S14, and the detailed calculation process of ECSA is reflected in the supporting information. FeNiO@NCNT has the highest C_{dl} value and the highest ECSA (17.17), superior to other catalysts, which is consistent with its superior performance.

In ORR region, CV and LSV tests were performed to evaluate the ORR performance of the prepared electrocatalysts on rotating disk electrodes in O_2-saturated 0.1 mol·L^{-1} KOH solution. As shown in Fig. S15, FeNiO@NCNT has a significant oxygen reduction peak potential at 0.8 V (vs. RHE), which is more positive than FeNi@NCNT (0.78 V). Within the LSV curve at 1600 r·min^{-1} (Fig. 3f), FeNiO@NCNT provides an onset potential (E_{onset}) of 0.9 V and a half-wave potential ($E_{1/2}$) of 0.75 V. The electron transfer number (n) of FeNiO@NCNT is calculated as 3.90, which is larger than that of the comparative catalysts (Fig. 3g), indicating that the 4e- ORR route is required for the catalytic process. The electrocatalyst has a K-L curve with good linear parallelism indicating a first-order reaction of catalytic oxygen (Fig. S16). The outstanding ORR activity of FeNiO@NCNT was evaluated by its lowest Tafel slope (52.8 mV·dec^{-1}) compared to FeNi@NCNT (65.3 mV·dec^{-1}), further highlighting its superior ORR kinetics (Fig. 3h).

With comprehensive comparison of OER and ORR performance, the performance of bimetallic catalysts is much better than that of single-metal catalysts. To further evaluate the activity of the bifunctional catalyst, it was further evaluated by the potential difference (ΔE) between $E_{j=10}$ of OER and $E_{1/2}$ of ORR. ΔE is obtained from equation $\Delta E = E_{j=10} - E_{1/2}$. Smaller ΔE corresponds to better overall oxygen catalytic activity. The OER potential ($E_{j=10}$) of FeNi@NCNT is 1.54 V, and the half-wave potential ($E_{1/2}$) of ORR is 0.72 V. The comprehensive calculation is: $\Delta E_{(FeNi@NCNT)} = E_{j=10} - E_{1/2} = 0.820$ V. The OER potential ($E_{j=10}$) of FeNiO@NCNT is 1.435 V, and the $E_{1/2}$ of ORR is 0.75 V. The comprehensive calculation is: $\Delta E_{(FeNiO@NCNT)} = E_{j=10} - E_{1/2} = 0.685$ V.

To further evaluate the performance of FeNiO@NCNT, it was compared with recently reported bimetallic FeNi catalysts (Fig. 3i). The results show that glu-NiFe (ΔE = 0.82 V) [82], FeNi/N–C-800 (ΔE = 0.755 V) [83], FeNi/N-CNT (ΔE = 0.757 V) [84] and FNSNC73-800 (ΔE = 0.82 V) [85] have larger ΔE than FeNiO@NCNT. Although the ORR performance of FeNiO@NCNT is worse than that of other samples, the extremely excellent OER performance makes its ΔE value much smaller than that of other samples, so the subsequent Zn–air battery test was carried out for evaluation.

Collecting the above results helps us to identify the excellent bifunctional electrocatalytic performance of

FeNiO@NCNT: First, the thicker and higher surface area of carbon nanotubes provides abundant and highly dispersed FeNiO active sites during OER/ORR process and promotes the mass diffusion and transport. Second, a higher proportion of pyridine nitrogen exists in FeNiO@NCNT, which is beneficial to increase the onset potential and limit the diffusion current. Third, the positive synergistic effect of bimetallic oxides and carbon nanotubes can improve electrical conductivity and ensure fast electron transport. Finally, the oxides of Fe and Ni encapsulated by carbon nanotubes endow the catalyst with better resistance to aggregation and dissolution.

To further evaluate the outstanding performance of the bifunctional catalyst FeNiO@NCNT, the liquid rechargeable Zn–air batteries were constructed, in which FeNiO@NCNT as air–cathode without external current corrector, polished zinc plate as the anode, and 6 mol·L^{-1} KOH with 0.2 mol·L^{-1} zinc acetate is used as the electrolyte (Fig. 4a). For comparison, the rechargeable Zn–air battery composed of same quality mixture of Pt/C and IrO_2 (1:1) was fabricated and investigated. As shown in Fig. 4b, c, the FeNiO@NCNT-based battery displays an open-circuit voltage of 1.38 V (close to that of Pt/IrO_2) and smaller discharge/charge gap than that of Pt/IrO_2 in the polarization curves. The FeNiO@NCNT-based Zn–air battery displays a higher discharge power density of 124.29 mW·cm^{-2}, which is 89.4 mW·cm^{-2} higher than that of the Pt/C + IrO_2-based battery (Fig. 4d). Moreover, the FeNiO@NCNT-based battery delivers a high specific capacity (per g of Zn) of 770.4 mAh·g_{Zn}^{-1} (Fig. S17). The recharge ability and cyclic stability that presented by charge–discharge cycle curves are shown in Fig. 4e, the charge and discharge voltages of FeNiO@NCNT-based battery without significant drop of the overpotential for more than 440 h. This shows that FeNiO@NCNT maintains a long-term stability with outstanding performance and is a very promising new catalyst. In particular, Table S3 shows the performance of FeNiO@NCNT compared with other Zn–air battery catalysts, which further confirms the excellent performance of FeNiO@NCNT.

In summary, MOF-derived MO@NCNT with N-doped nanotubes was successfully prepared as a highly active electrocatalyst, which possessed desirable merits such as superior conductivity, multiple active sites and large specific surface areas. The as-prepared FeNiO@NCNT exhibited more efficiently catalytic activities and improved durability toward both OER and ORR, which can be attributed to the nanotube structures with and the apical dominance of FeNi semi-oxidized metal particles encapsulated in the tip of the NCNT. In particular, the current density of 10 mA·cm^{-2} can be achieved with only 205 mV overpotential for OER, which is superior to most catalysts. The Zn–air batteries with both aqueous and solid electrolytes based on FeNiO@NCNT bifunctional air–cathode displayed low charging/discharging overpotential, high specific capacity and high-energy density. In addition, the battery exhibited excellent stability and durability further entitle FeNiO@NCNT as a desirable air–cathode catalyst,

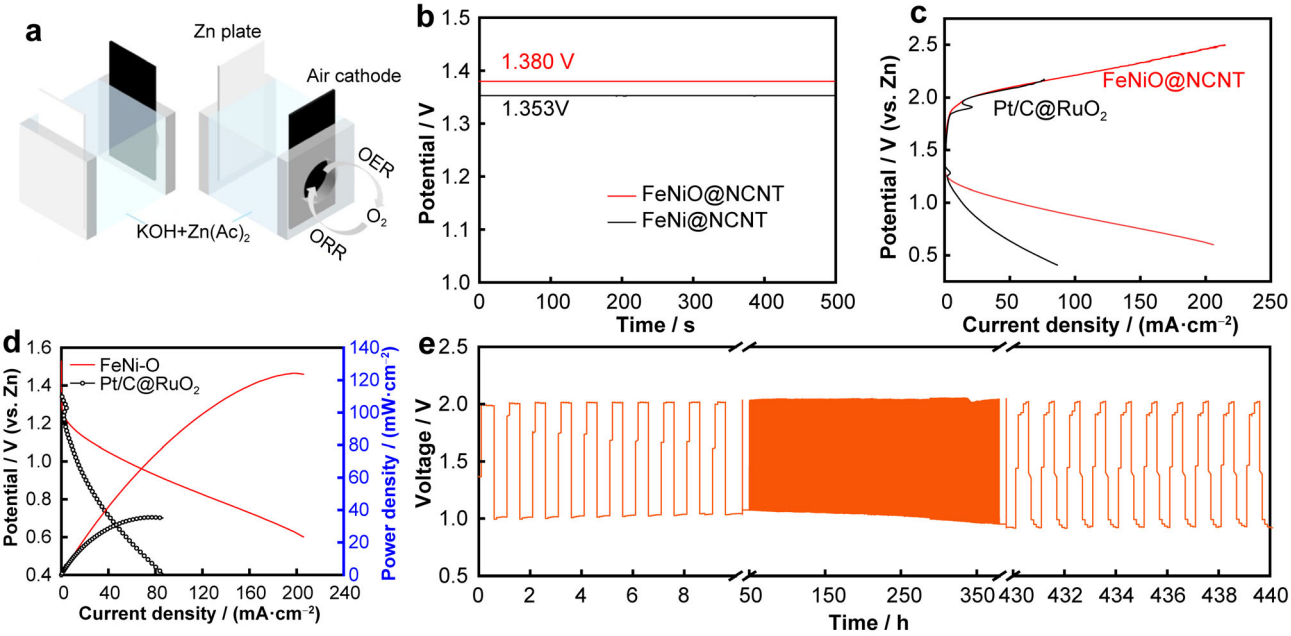

Fig. 4 Zn–air battery performance of FeNiO@NCNT compared with Pt/C@RuO_2 catalyst. **a** Schematic illustration of Zn–air battery, **b** open-circuit plots, **c** charge/discharge polarization curves, **d** polarization and power density curves and **e** long-term cycling performance at current density of 20 mA·cm^{-2} for 440 h

which provides a low-cost strategy and efficient bifunctional catalysts toward energy conversion devices.

Acknowledgements This work was financially supported by Zhejiang Provincial Natural Science Foundation of China (No. LY20E020001) and the Fundamental Research Funds of Zhejiang Sci-Tech University (No. 22212290-Y).

Declarations

Conflict of interests The authors declare that they have no conflict of interest.

References

[1] Zhu J, Chen XY, Thang AQ, Li FL, Chen D, Geng HB, Rui XH, Yan QY. Vanadiumbased metal-organic frameworks and their derivatives for electrochemical energy conversion and storage. SmartMat. 2022;3(3):384. https://doi.org/10.1002/smm2.1091.

[2] He B, Zhang QC, Pan ZH, Li L, Li CW, Ling Y, Wang ZX, Chen MX, Wang Z, Yao YG, Li QW, Sun LT, Wang J, Wei L. Freestanding metal-organic frameworks and their derivatives: an emerging platform for electrochemical energy storage and conversion. Chem Rev. 2022;122(11):10087. https://doi.org/10.1021/acs.chemrev.1c00978.

[3] Xu GY, Zhu CY, Gao G. Recent progress of advanced conductive metal-organic frameworks: precise synthesis, electrochemical energy storage applications, and future challenges. Small. 2022;18(44):2203140. https://doi.org/10.1002/smll.202203140.

[4] Zheng SB, Shi DJ, Yan D, Wang QR, Sun TJ, Ma T, Li L, He D, Tao ZL, Chen J. Orthoquinone-based covalent organic frameworks with ordered channel structures for ultrahigh performance aqueous zinc-organic batteries. Angew Chem Int Ed. 2022;61(12):17511. https://doi.org/10.1002/anie.202117511.

[5] Fan C, Wang X, Wu XR, Chen YS, Wang ZX, Li M, Sun DM, Tang YW, Fu GT. Neodymium-evoked valence electronic modulation to balance reversible oxygen electrocatalysis. Adv Energy Mater. 2022;13(2):2203244. https://doi.org/10.1002/aenm.202203244.

[6] Cai YL, Chen HW, Liu PX, Chen JZ, Xu H, Alshahrani T, Li LB, Chen BL, Gao JK. Robust microporous hydrogen-bonded organic framework for highly selective purification of methane from natural gas. Micropor Mesopor Mater. 2023;352:112495. https://doi.org/10.1016/j.micromeso.2023.112495.

[7] Yu DS, Ma YC, Hu F, Lin CC, Li LL, Chen HY, Han XP, Peng SJ. Dual-sites coordination engineering of single atom catalysts for flexible metal-air batteries. Adv Energy Mater. 2021;11(30):2101242. https://doi.org/10.1002/aenm.202101242.

[8] Vilas Bôas N, Souza Junior JB, Varanda LC, Machado SAS, Calegaro ML. Bismuth and cerium doped cryptomelane-type manganese dioxide nanorods as bifunctional catalysts for rechargeable alkaline metal-air batteries. Appl Catal B Environ. 2019;258:118014. https://doi.org/10.1016/j.apcatb.2019.118014.

[9] Liu HM, Liu QL, Wang YR, Wang YF, Chou SL, Hu ZZ, Zhang ZQ. Bifunctional carbonbased cathode catalysts for zinc-air battery: a review. Chin Chem Lett. 2022;33(2):683. https://doi.org/10.1016/j.cclet.2021.07.038.

[10] Deng YP, Jiang Y, Liang RL, Zhang SJ, Luo D, Hu YF, Wang X, Li JT, Yu AP, Chen ZW. Dynamic electrocatalyst with current-driven oxyhydroxide shell for rechargeable zinc-air battery. Nat Commun. 2020;11(1):1952. https://doi.org/10.1038/s41467-020-15853-1.

[11] Wang X, Wang JW, Wang P, Li LC, Zhang XY, Sun DM, Li YF, Tang YW, Wang Y, Fu GT. Engineering 3d–2p-4f gradient orbital coupling to enhance electrocatalytic oxygen reduction. Adv Mater. 2022;34(42):2206540. https://doi.org/10.1002/adma.202206540.

[12] Cui YF, Zhu YH, Du JY, Zhang YL, Li K, Liu WQ, Huang G, Zhang XB. A high-voltage and stable zinc-air battery enabled by dual-hydrophobic-induced proton shuttle shielding. Joule. 2022;6(7):1617. https://doi.org/10.1016/j.joule.2022.05.019.

[13] Yu JY, Chen FY, Tang Q, Gebremariam TT, Wang JL, Gong XF, Wang XL. Ag-modified Cu foams as three-dimensional anodes for rechargeable Zinc-Air batteries. Acs Appl Nano Mater. 2019;2(5):2679. https://doi.org/10.1021/acsanm.9b00156.

[14] Chen JJ, Gu S, Hao R, Wang ZY, Li MQ, Li ZQ, Liu K, Liao KM, Wang ZQ, Huang H, Li YZ, Zhang KL, Lu ZG. Co single atoms and nanoparticles dispersed on N-doped carbon nanotube as high-performance catalysts for Zn-air batteries. Rare Met. 2022;41(6):2055. https://doi.org/10.1007/s12598-022-01974-7.

[15] Khan U, Nairan A, Gao JK, Zhang QC. Current progress in 2D metal-organic frameworks for electrocatalysis. Small Struct. 2023;4(6):2200109. https://doi.org/10.1002/sstr.202200109.

[16] Song M, Zhong CL. Achieving both high reversible and stable Zn anode by a practical glucose electrolyte additive toward high-performance Zn-ion batteries. Rare Met. 2021;41(2):356. https://doi.org/10.1007/s12598-021-01858-2.

[17] Cheng WZ, Liang JL, Yin HB, Wang YJ, Yan WF, Zhang JN. Bifunctional iron-phtalocyanine metal-organic framework catalyst for ORR, OER and rechargeable zinc-air battery. Rare Met. 2020;39(7):815. https://doi.org/10.1007/s12598-020-01440-2.

[18] Sun C, Zhao YJ, Yuan XY, Li JB, Jin HB. Bimetal nanoparticles hybridized with carbon nanotube boosting bifunctional oxygen electrocatalytic performance. Rare Met. 2022;41(8):2616. https://doi.org/10.1007/s12598-022-02021-1.

[19] Su DC, Xiao YH, Liu YL, Xu SG, Fang SM, Cao SK, Wang XZ. Surface-confined polymerization to construct binary Fe_3N/Co-N-C encapsulated MXene composites for high-performance zinc-air battery. Carbon. 2023;201:269. https://doi.org/10.1016/j.carbon.2022.09.007.

[20] He YT, Yang XX, Li YS, Liu LT, Guo SW, Shu CY, Liu F, Liu YN, Tan Q, Wu G. Atomically dispersed Fe–Co dual metal sites as bifunctional oxygen electrocatalysts for rechargeable and flexible Zn–Air batteries. ACS Catal. 2022;12(2):1216. https://doi.org/10.1021/acscatal.1c04550.

[21] Liu XR, Yuan YF, Liu J, Liu B, Chen X, Ding J, Han XP, Deng YD, Zhong C, Hu WB. Utilizing solar energy to improve the oxygen evolution reaction kinetics in zinc-air battery. Nat Commun. 2019;10(1):4767. https://doi.org/10.1038/s41467-019-12627-2.

[22] Shang N, Wang KL, Wei MH, Zuo YY, Zhang PF, Wang HW, Chen Z, Pei PC. Challenges for large scale applications of rechargeable Zn-air batteries. J Mater Chem A. 2022;10(31):16369. https://doi.org/10.1039/d2ta04294k.

[23] Zhao RP, Chen ZH, Li QH, Wang X, Tang YW, Fu GT, Li H, Lee JM, Huang SM. Ndoped $LaPO_4$: an effective Pt-free catalyst for electrocatalytic oxygen reduction. Chem Catal. 2022;2(12):3590. https://doi.org/10.1016/j.checat.2022.11.008.

[24] Gou WY, Xia ZM, Tan XH, Xue QY, Ye F, Dai S, Zhang MK, Si R, Zou Y, Ma YY, Ho JC, Qu YQ. Highly active and stable amorphous IrO_x/CeO_2 nanowires for acidic oxygen evolution. Nano Energy. 2022;104:107960. https://doi.org/10.1016/j.nanoen.2022.107960.

[25] Liu DP, Zhang J, Liu DD, Li TZ, Yan YD, Wei XY, Yang YD, Yan SC, Zou ZG. N-doped graphene-coated commercial Pt/C catalysts toward high-stability and antipoisoning in oxygen

reduction reaction. J Phys Chem Lett. 2022;13(8):2019. https://doi.org/10.1021/acs.jpclett.1c04005.
[26] Li YW, Wu YH, Li TT, Lu MT, Chen Y, Cui YJ, Gao JK, Qian GD. Tuning the electronic structure of a metal-organic framework for an efficient oxygen evolution reaction by introducing minor atomically dispersed ruthenium. Carbon Energy. 2023;5:e265. https://doi.org/10.1002/cey2.265.
[27] Deng BL, Guo LP, Lu Y, Rong HB, Cheng DC. Sulfur-nitrogen co-doped graphene supported cobalt–nickel sulfide rGO@SN--$CoNi_2S_4$ as highly efficient bifunctional catalysts for hydrogen/oxygen evolution reactions. Rare Met. 2021;41(3):911. https://doi.org/10.1007/s12598-021-01828-8.
[28] Fu J, Liang RL, Liu GH, Yu AP, Bai ZY, Yang L, Chen ZW. Recent progress in electrically rechargeable zinc-air batteries. Adv Mater. 2019;31(31):1805230. https://doi.org/10.1002/adma.201805230.
[29] Xiao X, Zhao H, Li LF, Qu BL, Wu YL, Zhu YL, Chen BB, Pan G. Ion exchange coupled biomineral self-sacrificial template synthesis of N-enriched porous carbon as robust electrocatalyst for rechargeable Zn-air battery. Rare Met. 2023;42(4):1186. https://doi.org/10.1007/s12598-022-02190-z.
[30] Gao JK, Huang Q, Wu YH, Lan YQ, Chen BL. Metal-organic frameworks for photo/electrocatalysis. Adv Energy Sustain Res. 2021;2(8):2100033. https://doi.org/10.1002/aesr.202100033.
[31] Vijayakumar E, Ramakrishnan S, Sathiskumar C, Yoo DJ, Balamurugan J, Noh HS, Kwon D, Kim YH, Lee H. MOF--derived CoP-nitrogen-doped carbon@NiFeP nanoflakes as an efficient and durable electrocatalyst with multiple catalytically active sites for OER, HER, ORR and rechargeable zinc-air batteries. Chem Eng J. 2022;428:131115. https://doi.org/10.1016/j.cej.2021.131115.
[32] Gaur A, Pundir V, Krishankant Rai R, Kaur B, Maruyama T, Bera C, Bagchi V. Interfacial interaction induced OER activity of MOF derived superhydrophilic Co_3O_4-NiO hybrid nanostructures. Dalton Trans. 2022;51(5):2019. https://doi.org/10.1039/d1dt03810a.
[33] Singh H, Marley-Hines M, Chakravarty S, Nath M. Multi-walled carbon nanotube supported manganese selenide as a highly active bifunctional OER and ORR electrocatalyst. J Mater Chem A. 2022;10(12):6772. https://doi.org/10.1039/d1ta09864k.
[34] Guo YM, Zhang LJ, XiLi DG, Kang J. Advances of carbon materials as loaders for transition metal oxygen/sulfide anode materials. Chin J Rare Met. 2021;45(10):1241. https://doi.org/10.13373/j.cnki.cjrm.XY20040016
[35] Chang HY, Liang ZJ, Wang L, Wang C. Research progress in improving the oxygen evolution reaction by adjusting the 3d electronic structure of transition metal catalysts. Nanoscale. 2022;14(15):5639. https://doi.org/10.1039/d2nr00522k.
[36] Zhang MT, Li H, Chen JX, Ma FX, Zhen L, Wen ZH, Xu CY. Transition metal (Co, Ni, Fe, Cu) single-atom catalysts anchored on 3D nitrogen-doped porous carbon nanosheets as efficient oxygen reduction electrocatalysts for Zn-air battery. Small. 2022;18(34):2202476. https://doi.org/10.1002/smll.202202476.
[37] Yu L, Li F, Zhao J, Chen Z. Revisiting catalytic performance of supported metal dimers for oxygen reduction reaction via magnetic coupling from first principles. Adv Powder Mater. 2022;1(3):100031. https://doi.org/10.1016/j.apmate.2022.01.004.
[38] Chen HX, Xu H, Song ZR, Liu Y, Cui H, Gao JK. Pressure-induced bimetallic carbon nanotubes from metal–organic frameworks as optimized bifunctional electrocatalysts for water splitting. Rare Met. 2022;42(1):155. https://doi.org/10.1007/s12598-022-02121-y.
[39] Pan Y, Gao J, Lv E, Li T, Xu H, Sun L, Nairan A, Zhang Q. Integration of alloy segregation and surface Co-O hybridization in carbon-encapsulated CoNiPt alloy catalyst for superior alkaline hydrogen evolution. Adv Funct Mater. 2023;33:2303833. https://doi.org/10.1002/adfm.202303833.
[40] Liu FQ, Peng H, Kang YM, Hao YX, Li LF, Xin HY, Kang HC, Wang W, Lei ZQ. Rare-earth-based bimetallic metal-organic frameworks promote oxygen electrocatalysis for rechargeable Zn–Air batteries. ACS Sustain Chem Eng. 2022;10(33):10978. https://doi.org/10.1021/acssuschemeng.2c03045.
[41] Chen X, Pu J, Hu XH, An L, Jiang JJ, Li YJ. Confinement synthesis of bimetallic MOF-derived defect-rich nanofiber electrocatalysts for rechargeable Zn-air battery. Nano Res. 2022;15(10):9000. https://doi.org/10.1007/s12274-022-4563-4.
[42] Wu YH, Li YW, Gao JK, Zhang QC. Recent advances in vacancy engineering of metalorganic frameworks and their derivatives for electrocatalysis. SusMat. 2021;1(1):66. https://doi.org/10.1002/sus2.3.
[43] Guo SQ, Sun YX, Wang JN, Peng LC, Li HY, Li CJ. Bimetallic ZIF-derived cobalt nanoparticles anchored on N- and S-codoped porous carbon nanofibers as cathode catalyst for Li-O_2 batteries. Electrochim Acta. 2022;418:140279. https://doi.org/10.1016/j.electacta.2022.140279.
[44] HyounAhn C, Seok Yang W, Jae Kim J, Sudha Priyanga G, Thomas T, Deshpande NG, Seong Lee H, Koun Cho H. Design of hydrangea-type Co/Mo bimetal MOFs and MOF-derived Co/Mo_2C embedded carbon composites for highly efficient oxygen evolution reaction. Chem Eng J. 2022;435:134815. https://doi.org/10.1016/j.cej.2022.134815.
[45] You B, Jiang N, Sheng ML, Drisdell WS, Yano JK, Sun YJ. Bimetal-wuction. ACS Catal. 2015;5(12):7068. https://doi.org/10.1021/acscatal.5b02325.
[46] Ma XF, Xiong Y, Liu YS, Han JQ, Duan GG, Chen YM, He SJ, Mei CT, Jiang SH, Zhang K. When MOFs meet wood: from opportunities toward applications. Chem. 2022;8(9):2342. https://doi.org/10.1016/j.chempr.2022.06.016.
[47] Liu DB, Ding SQ, Wu CQ, Gan W, Wang CD, Cao DF, Rehman Zu, Sang Y, Chen SM, Zheng XS, Wang Y, Ge BH, Song L. Synergistic effect of an atomically dual-metal doped catalyst for highly efficient oxygen evolution. J Mater Chem A. 2018;6(16):6840. https://doi.org/10.1039/c8ta00550h.
[48] Li YW, Zhao T, Lu MT, Wu YH, Xie YB, Xu H, Gao JK, Yao JM, Qian GD, Zhang QC. Enhancing oxygen evolution reaction through modulating electronic structure of trimetallic electrocatalysts derived from metal-organic frameworks. Small. 2019;15(43):1901940. https://doi.org/10.1002/smll.201901940.
[49] Acharya D, Pathak I, Dahal B, Lohani PC, Bhattarai RM, Muthurasu A, Kim T, Ko TH, Chhetri K, Kim HY. Immoderate nanoarchitectures of bimetallic MOF derived Ni-Fe-O/NPC on porous carbon nanofibers as freestanding electrode for asymmetric supercapacitors. Carbon. 2023;201:12. https://doi.org/10.1016/j.carbon.2022.08.091.
[50] Kiran S, Yasmeen G, Shafiq Z, Abbas A, Manzoor S, Hussain D, Adel Pashameah R, Alzahrani E, Alanazi AK, Naeem AM. Nickel-based nitrodopamine MOF and its derived composites functionalized with multi-walled carbon nanotubes for efficient OER applications. Fuel. 2023;331:125881. https://doi.org/10.1016/j.fuel.2022.125881.
[51] He MM, Zhang P, Huo SL, Zhang XL, Gong A, Zhang W, Li KX. Remarkable phosphate electrosorption/desorption by bimetallic MOF-derived hierarchically porous carbon electrode: In-situ creation of multiple active centers and boosting electrochemical activities. Chem Eng J. 2022;446:137396. https://doi.org/10.1016/j.cej.2022.137396.
[52] Han X, Zhang TY, Wang XH, Zhang ZD, Li Y, Qin YP, Wang BQ, Han AJ, Liu JF. Hollow mesoporous atomically dispersed metal-nitrogen-carbon catalysts with enhanced diffusion for catalysis involving larger molecules. Nat Commun. 2022;13(1):2900. https://doi.org/10.1038/s41467-022-30520-3.

[53] Wang JW, Sun Y, Zhao XM, Chen L, Peng SY, Ma CX, Duan GG, Liu ZZ, Wang H, Yuan YH, Wang N. A poly(amidoxime)-modified MOF macroporous membrane for higheffi-cient uranium extraction from seawater. e-Polymers. 2022;22(1):399. https://doi.org/10.1515/epoly-2022-0038.
[54] Ma XF, Zhao SY, Tian ZW, Duan GG, Pan HY, Yue YY, Li SS, Jian SJ, Yang WS, Liu KM, He SJ, Jiang SH. MOFs meet wood: reusable magnetic hydrophilic composites toward efficient water treatment with super-high dye adsorption capacity at high dye concentration. Chem Eng J. 2022;446:136851. https://doi.org/10.1016/j.cej.2022.136851.
[55] Du YX, Zhou YT, Zhu MZ. Co-based MOF derived metal catalysts: from nano-level to atom-level. Tungsten. 2023;5:201. https://doi.org/10.1007/s42864-022-00197-8.
[56] Ma SY, Han WG, Han WL, Dong F, Tang ZC. Recent advances and future perspectives in MOF-derived single atom catalysts and their application: a review. J Mater Chem A. 2023;11:3315. https://doi.org/10.1039/d2ta08735a.
[57] Gao Z, Lai YL, Gong LL, Zhang LP, Xi SB, Sun J, Zhang LJ, Luo F. Robust Th-MOF-supported semirigid single-metal-site catalyst for an efficient acidic oxygen evolution reaction. ACS Catal. 2022;12(15):9101. https://doi.org/10.1021/acscatal.2c02181.
[58] Meng ZH, Zhu G, Wu JW, Wang R, Tian T, Tang HB, Luo R, Ye DH, Zhang RM, Kwofie F, Cheng Y, Tang HL. Gradient Co/Zn bimetallic coordinated polymer-derived hierarchically porous carbon for boosted oxygen electrocatalysts of rechargeable Zn-air batteries. Mater Today Energy. 2022;24:100935. https://doi.org/10.1016/j.mtener.2021.100935.
[59] Wang ZC, Hou XT, Dekyvere S, Mousavi B, Chaemchuen S. Single-thermal synthesis of bimetallic Co/Zn@NC under solvent-free conditions as an efficient dualfunctional oxygen electrocatalyst in Zn-air batteries. Nanoscale. 2022;14(44):16683. https://doi.org/10.1039/d2nr03997d.
[60] Naveed A, Li GT, Ali A, Li MY, Wan T, Hassan M, Wang X, Ye P, Li XW, Zhou Y, Su MR, Guo RQ, Liu YJ, Xu HL, Chu DW. Realizing high reversibility and safety of Zn anode via binary mixture of organic solvents. Nano Energy. 2023;107:108175. https://doi.org/10.1016/j.nanoen.2023.108175.
[61] Wang XR, Naveed A, Zeng TY, Wan T, Zhang HW, Zhou Y, Dou AC, Su MR, Liu YJ, Chu DW. Sodium ion stabilized ammonium vanadate as a high-performance aqueous zinc-ion battery cathode. Chem Eng J. 2022;446:137090. https://doi.org/10.1016/j.cej.2022.137090.
[62] Manna SC, Ghosh AK, Ribas J, Drew MGB, Lin CN, Zangrando E, Ray CN. Synthesis, crystal structure, magnetic behavior and thermal property of three polynuclear complexes: $[M(dca)_2(H_2O)_2]_n \cdot (hmt)_n$ [M=Mn(II), Co(II)] and $[Co(dca)_2(bpds)]_n$ [dca, dicyanamide; hmt, hexamethylenetetramine; bpds, 4,4'-bipyridyl disulfide]. Inorg Chim Acta. 2006;359(5):1395. https://doi.org/10.1016/j.ica.2005.09.035.
[63] Wu YH, Li YW, Zhao T, Wang X, Isaeva VI, Kustov LM, Yao JM, Gao JK. Bimetalorganic framework-derived nanotube@-cellulose aerogels for peroxymonosulfate (PMS) activation. Carbohydr Polym. 2022;296:119969. https://doi.org/10.1016/j.carbpol.2022.119969.
[64] Lu Q, Yu J, Zou XH, Liao KM, Tan P, Zhou W, Ni M, Shao ZP. Self-catalyzed growth of Co, N-codoped CNTs on carbon-encased CoS_x surface: a noble-metal-free bifunctional oxygen electrocatalyst for flexible solid Zn-air batteries. Adv Funct Mater. 2019;29(38):1904481. https://doi.org/10.1002/adfm.201904481.
[65] Liu N, Dou YY, Zhang XY, Yu LM, Yan XF. Design of porous FeNi-carbon nanosheets by a double-effect synergistic strategy for electromagnetic wave absorption. Carbon. 2022;190:125. https://doi.org/10.1016/j.carbon.2022.01.007.
[66] Guo XY, Yao L, Hou XY, Wu XF, Zhang YW, Zhu Q, Guo ZT, Li ST, Jiang YL, Feng SH, Huang KK. An exsolution constructed FeNi/$NiFe_2O_4$ composite: preferential breaking of octahedral metal-oxygen bonds in a spinel oxide. Chem Sci. 2022;13(32):9440. https://doi.org/10.1039/d2sc02149h.
[67] Su H, Tang YQ, Shen HM, Zhang H, Guo PH, Gao L, Zhao X, Xu XS, Li SQ, Zou RQ. Insights into antiperovskite $Ni_3In_{1-x}Cu_xN$ multi-crystalline nanoplates and bulk cubic particles as efficient electrocatalysts on hydrogen evolution reaction. Small. 2022;18(12):2105906. https://doi.org/10.1002/smll.202105906.
[68] Wang Y, Gong YS, Lin NP, Jiang H, Wei X, Liu N, Zhang XD. Cellulose hydrogel coated nanometer zero-valent iron intercalated montmorillonite (CH-MMT-nFe^0) for enhanced reductive removal of Cr(VI): characterization, performance, and mechanisms. J Mol Liq. 2022;347:118355. https://doi.org/10.1016/j.molliq.2021.118355.
[69] Zhou YH, Xiong WM, Jin YJ, Wang P, Wei WQ, Ma JL, Zhang XH. Catalytic aerobic oxidation of lignin-based vanillyl alcohol under base–free conditions over an efficient and reusable $LaFeO_3$ perovskite for vanillin production. Green Chem. 2023;25:1179. https://doi.org/10.1039/d2gc04132d.
[70] Thambiliyagodage C, Usgodaarachchi L, Jayanetti M, Liyanaarachchi C, Kandanapitiye M, Vigneswaran S. Efficient visible-light photocatalysis and antibacterial activity of TiO_2-Fe_3C-Fe-Fe_3O_4/graphitic carbon composites fabricated by catalytic graphitization of sucrose using natural ilmenite. ACS Omega. 2022;7(29):25403. https://doi.org/10.1021/acsomega.2c02336.
[71] Zeng F, Zhang J, Xu R, Zhang RJ, Ge JP. Highly dispersed Ni/MgO-$mSiO_2$ catalysts with excellent activity and stability for dry reforming of methane. Nano Res. 2022;15(6):5004. https://doi.org/10.1007/s12274-022-4180-2.
[72] Ding YL, Wang MY, Mei ZY, Liu L, Yang JM, Zhong XL, Wang M, Diao XG. Electrochromic adaptability of NiO_x films modified by substrate temperature inaqueous and non-aqueous electrolytes. Adv Mater Inter. 2022;9(17):2102223. https://doi.org/10.1002/admi.202102223.
[73] Yang GZ, Chen B, Zhao WQ, Xu MH, Lu Y, Xue YH, Zhang HJ. Nitrogen, sulfur and fluorine tri-doped carbon supporting cobalt nanoparticles for oxygen reduction catalysis. J Electrochem Soc. 2022;169(3):034501. https://doi.org/10.1149/1945-7111/ac5792.
[74] Yang CT, Feng H, Chen XB, Han Y, Li HB, Xu DK, Wang FH. Enhanced pitting corrosion resistance of CoCrFeMnNi high entropy alloy in the presence of Desulfovibrio vulgaris via nitrogen doping. J Mater Sci Technol. 2023;139:92. https://doi.org/10.1016/j.jmst.2022.08.021.
[75] Deng WH, Wu TJ, Wu YF, Zheng HT, Li G, Yang MX, Zou XQ, Bai YS, Yang YC, Jing MJ, Wang XY. Single atomic Fe-pyridine N catalyst with dense active sites improve bifunctional electrocatalyst activity for rechargeable and flexible Zn-air batteries. J Mater Chem A. 2022;10(39):20993. https://doi.org/10.1039/d2ta06351d.
[76] Zhang SQ, Qin YP, Zhu J, Hou JH. Over 14% efficiency in polymer solar cells enabled by a chlorinated polymer donor. Adv Mater. 2018;30(20):1800868. https://doi.org/10.1002/adma.201800868.
[77] Wang XX, You FF, Wen XY, Wang KR, Tong GX, Wu WH. Doping $Ce(OH)CO_3$ laminated dendrites with Fe, Co and Ni for defect steered wide-frequency microwave absorption. Chem Eng J. 2022;445:136431. https://doi.org/10.1016/j.cej.2022.136431.
[78] Shan JQ, Ling T, Davey K, Zheng Y, Qiao SZ. Transition-metal-doped ruir bifunctional nanocrystals for overall water splitting in acidic environments. Adv Mater. 2019;31(17):1900510. https://doi.org/10.1002/adma.201900510.

[79] Zhang CY, Wang AX, Guo LY, Yi J, Luo JY. A moisture-assisted rechargeable Mg-CO_2 battery. Angew Chem Int Ed. 2022; 61(17):00181. https://doi.org/10.1002/anie.202200181.
[80] Bezerra LS, Maia G. Developing efficient catalysts for the OER and ORR using a combination of Co, Ni, and Pt oxides along with graphene nanoribbons and $NiCo_2O_4$. J Mater Chem A. 2020;8(34):17691. https://doi.org/10.1039/d0ta05908k.
[81] Fabbri E, Schmidt TJ. Oxygen evolution reaction-the enigma in water electrolysis. ACS Catal. 2018;8(10):9765. https://doi.org/10.1021/acscatal.8b02712.
[82] Chen X, Chen D, Li GF, Sha PF, Yu JH, Yu LY, Dong LF. FeNi incorporated N doped carbon nanotubes from glucosamine hydrochloride as highly efficient bifunctional catalyst for long term rechargeable zinc-air batteries. Electrochim Acta. 2022; 428:140938. https://doi.org/10.1016/j.electacta.2022.140938.
[83] Xiong Q, Zheng JH, Liu B, Liu YJ, Li HM, Yang M. In-situ self-templating construction of FeNi/N co-doped 3D porous carbon from bimetallic ions-coordinated porous organic polymer for rechargeable zinc-air batteries. Appl Catal B Environ. 2023; 321:122067. https://doi.org/10.1016/j.apcatb.2022.122067.
[84] Zheng JH, Kang TJ, Liu B, Wang P, Li H, Yang M. N-doped carbon nanotubes encapsulated with FeNi nanoparticles derived from defect-rich, molecule-doped 3D g-C_3N_4 as an efficient bifunctional electrocatalyst for rechargeable zinc–air batteries. J Mater Chem A. 2022;10(18):9911. https://doi.org/10.1039/d2ta00750a.
[85] Wu R, Wang XX, Ge L, Zheng ZH, Zhu YJ, Zhou C, Yuan JL, Zhu SL, Gu YX, Zhou W, Shao ZP. N, S co-doped carbon with embedment of FeNi alloy as bifunctional oxygen electrocatalysts for rechargeable zinc-air batteries. Carbon. 2023;202:141. https://doi.org/10.1016/j.carbon.2022.10.047.